

Stellar flare study of nearby young moving group members with TESS Data

ANDREW TRAN¹ AND INSEOK SONG¹

¹*Department of Physics and Astronomy, University of Georgia
Sanford Dr. Athens, GA, 30606, USA*

ABSTRACT

We analyze TESS data to explore stellar flares and rotational characteristics in members of Nearby Young Moving Groups (NYMGs). Our study focuses on 417 members of NYMGs aged 10-150 Myr. Using detrended light curves from the TESS Science Office Quick-Look Pipeline, coupled with our own additional detrending scheme for fast rotators, we systematically detect and characterize 6,288 stellar flares from 27,416 flare candidates. We analyzed light curves from Cycles 1-4 of the TESS mission, finding that for each NYMG member analyzed, at least one stellar flare was present. Flare candidates are initially detected using the AltaiPony flare package, followed by a recovery flare amplitudes, durations, and local continuum background levels. We examine the relationship between flare energy, age, and mass, finding a reduced flaring rate for late-type stars with age for high energy flares, as well as 5.5 times more flares detected in the 10-minute cadence TESS data compared to 30-minute cadence data. Additionally, flare events with extreme energies ($E \geq 10^{34}$ erg) on M-dwarf and solar-type stars, providing implications for further exploration into exoplanet habitability.

Keywords: flares — moving groups — TESS — stars: young

1. INTRODUCTION

Nearby young moving groups (NYMGs) are gravitationally unbound groups of stars with the same relative motion in the age range of 10 Myr to 200 Myr and within ≈ 100 pc from the Sun. These groups are critical for studying the early stages of stellar and planetary evolution due to their youth (≤ 200 Myr) and proximity (≈ 100 pc), which allow for detailed observations and analyses of stellar formation processes, disk evolution, and planet formation dynamics (Torres et al. 2008; Zuckerman et al. 2011). NYMG studies have provided valuable insights into stellar evolution in these associations (Zuckerman & Song 2004) and have contributed to more reliable age-dating methods, (Lee et al. 2022; Barrado y Navascués et al. 1999; Gagné et al. 2017). Additionally, NYMG members, such as those in the β Pictoris Moving Group, have historically been prime candidates for studying planetary system formation (Zuckerman et al. 2001). These groups are valuable for direct imaging and spectroscopy of young planets, offering insights into planet formation processes that are inconceivable currently in older systems (Marley et al. 2007; Macintosh et al. 2015). Furthermore, their homogeneous environment facilitates accurate determinations of stellar properties, such as chemical abundances, which are essential for contextualizing any exoplanets discovered (Spiegel & Burrows 2012). NYMGs also provide a near-complete census of low-mass M-dwarf stars, which are of significant interest for habitable planet studies (Dressing & Charbonneau 2013; Henry et al. 2006).

Stellar flares, which are sudden releases of energy due to magnetic reconnection events, are crucial in understanding the magnetic, rotational, and exoplanet-related characteristics (such as the effect of flares on the atmosphere's chemical composition) of stars (Davenport et al. 2019). Flares are particularly important for investigating the conditions necessary for planetary habitability, as they influence the atmospheric chemistry and magnetic environment of exoplanets (Hazra et al. 2021). Previous studies utilizing photometric data from surveys like Kepler (Davenport et al. 2019) and the Transiting Exoplanet Survey Satellite (TESS) (Ricker et al. 2014) have provided a wealth of information on flare activity in young stars. Recent works have focused on characterizing flares across various spectral types and ages to better understand the magnetic environments in which planets form (Feinstein et al.

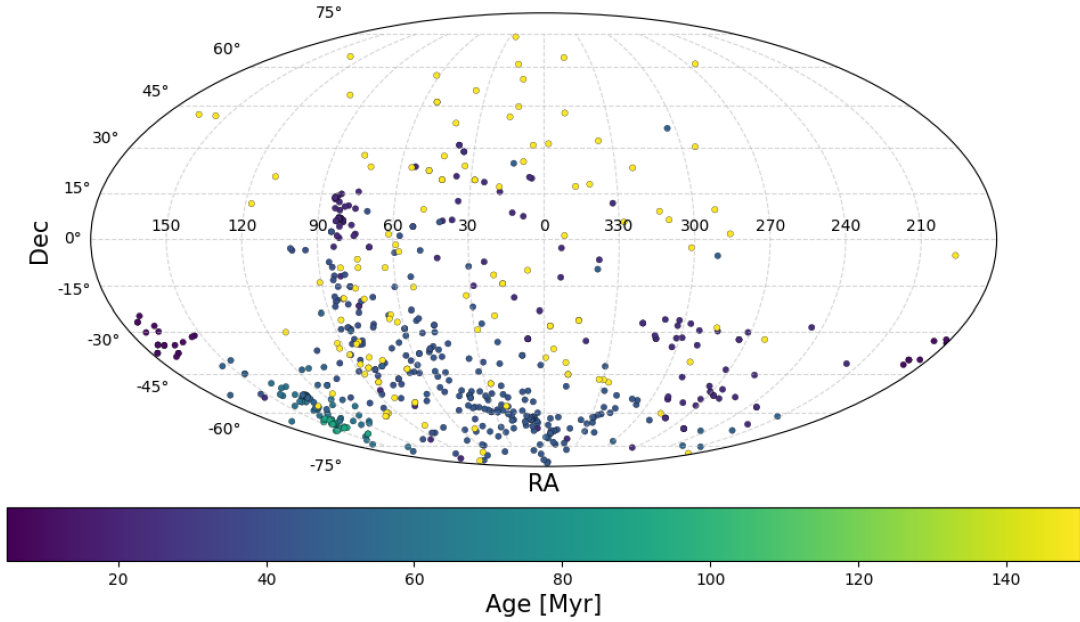


Figure 1. Distribution of the selected NYMG sample in the sky that had QLP data available for download, color coded by age of the associated moving group.

2020). Additionally, coronal mass ejections and flares are thought to have significant impacts on Jovian-like exoplanets (Howard & Law 2021), and flare frequency distributions (FFDs) have been used as a tool to investigate coronal heating mechanisms (Verbeeck et al. 2019).

While previous studies have laid the groundwork for understanding flare activity, particularly in M-dwarfs and other low-mass stars, gaps remain in comprehensively characterizing flares in younger populations. For instance, the flaring rate reaches its peak for M5-M7 stars but drastically diminishes for cooler M-dwarfs (Murray et al. 2022). This decline is thought to reduce the potential for photosynthetic processes on surrounding exoplanets (Feinstein et al. 2020). Caldiroli et al. (2025) similarly found that M-dwarf flares have a minimal effect on the atmospheric retention of Neptune-size planets, including ones in the habitable zones of their stars. In G-type stars, studies have found that superflares—events with energies larger than 10^{33} ergs—occur not only on fast rotators but also on slow rotators with periods comparable to that of the Sun (Crowley et al. 2022), corroborating earlier findings (Maehara et al. 2012). Additionally, flare energies and durations in M-dwarfs have been found to follow scaling laws similar to those of solar white light flares (Paudel et al. 2024), suggesting common underlying physical processes.

In this work, we offer additional insights over previous flare investigations. First, while recent work has primarily focused on older stellar populations, our study centers on stars in NYMGs within the 10-150 Myr age range, using the membership list from Lee & Song (2019), and utilizing 30 minute and 10 minute cadence TESS minute data.

We apply comprehensive flare detection procedures across light curves from members of nine NYMGs, spanning multiple observation sectors from four TESS cycles (2018-2023). By categorizing our sample by moving group (age) and spectral type, we investigate cumulative flare frequency distributions (FFDs) and as well as relationships between flaring activity and various astrophysical parameters. Our analysis provides further sampling and insights into the behavior and characteristics of stellar populations in the 10-150 Myr age range, adding valuable data to the ongoing study of stellar and planetary evolution in NYMGs.

2. DATA AND METHODOLOGY

2.1. TESS Data

We utilized data from the first four observation cycles (2018-2023) of the Transiting Exoplanet Survey Satellite (TESS), where Cycles 1-2 correspond to 30-minute cadence data, and Cycles 3-4 correspond to 10-minute cadence data. The distribution of the NYMG members with available TESS lightcurves is shown in Figure 1, with the majority of the members concentrated in southern declinations, due to the distribution of NYMGs. By cross-matching the list of NYMGs (Lee & Song 2019) in MAST for matching TESS data, we initially identified 2,240 TESS light curves and downloaded them, and removed contaminated cases, using the following relation from Rebull et al. (2022):

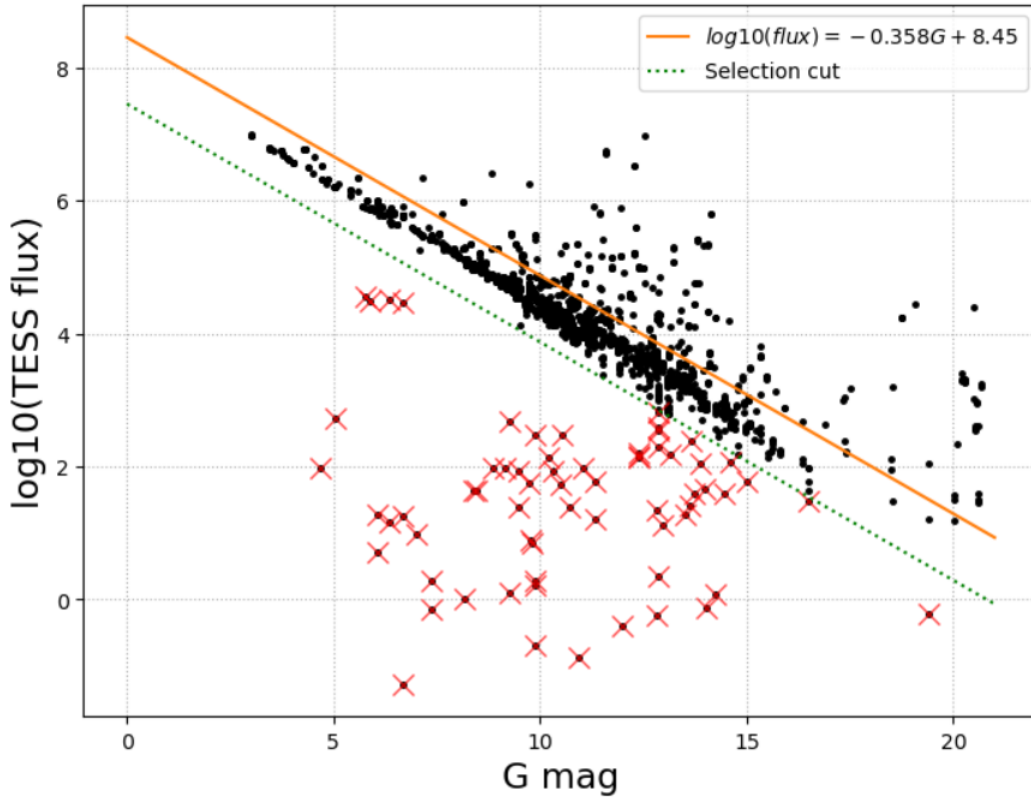


Figure 2. The contamination plot for the TESS data in this study. Data points lying above the orange line are potential contaminants, as they have additional stars in the TESS aperture so that for a given G-band magnitude, we see higher flux values. Data points marked with a red 'X' potentially contain interference from non-astrophysical sources.

$$\log(\text{mean LC flux}) = -0.358 \times G + 8.45 \quad (1)$$

This relation provides a predictive model for estimating TESS instrumental flux (in units of $e^- \text{sec}^{-1}$) from **Gaia DR2**'s G-band magnitude. The results from applying this relation to our sample are displayed in Figure 2. In this figure, points lying above the orange curve are inconsistent with what would be expected from their G-magnitudes, implying TESS fluxes were affected from background stars (Rebull et al. 2022). The green dashed line represents the selection cut used to remove likely contaminated apertures. It was defined as an offset of 0.65 dex below the best-fit flux–magnitude relation to exclude targets with excess TESS flux relative to their G-band magnitude. Additionally, stars below this cut recorded too low TESS fluxes for given Gaia brightness indicating unreliable TESS measurements for these stars. Upon closer examinations, TESS photometric data for these sources were affected by events such as the bright diffraction spikes from adjacent bright stars, etc. We removed stars above the orange line or below the green line. In total, we removed 378 contaminated light curves.

2.2. Light Curves

We used light curves from the TESS Science Center's Quick-Look Pipeline (QLP). We were able to cross-match and retrieve light curves for 417 stars between our membership list and the available QLP sample. In general, most of the raw light curve exhibited a variable, sinusoidal-like rotation-modulated variability with respect to time, allowing us to recover a rotational period as well. However, many light curves (LCs) detrended by the QLP pipeline were insufficiently detrended or possibly not detrended at all, particularly for fast rotators. This issue could have affected the flare identification process. To remove the remaining rotational signals in QLP LCs, we applied a Hampel-based rolling median filter to all light curves with estimated rotational periods less than 0.6 days, obtained from each star's Lomb-Scargle Periodogram, to remove the stellar baseline, then used median

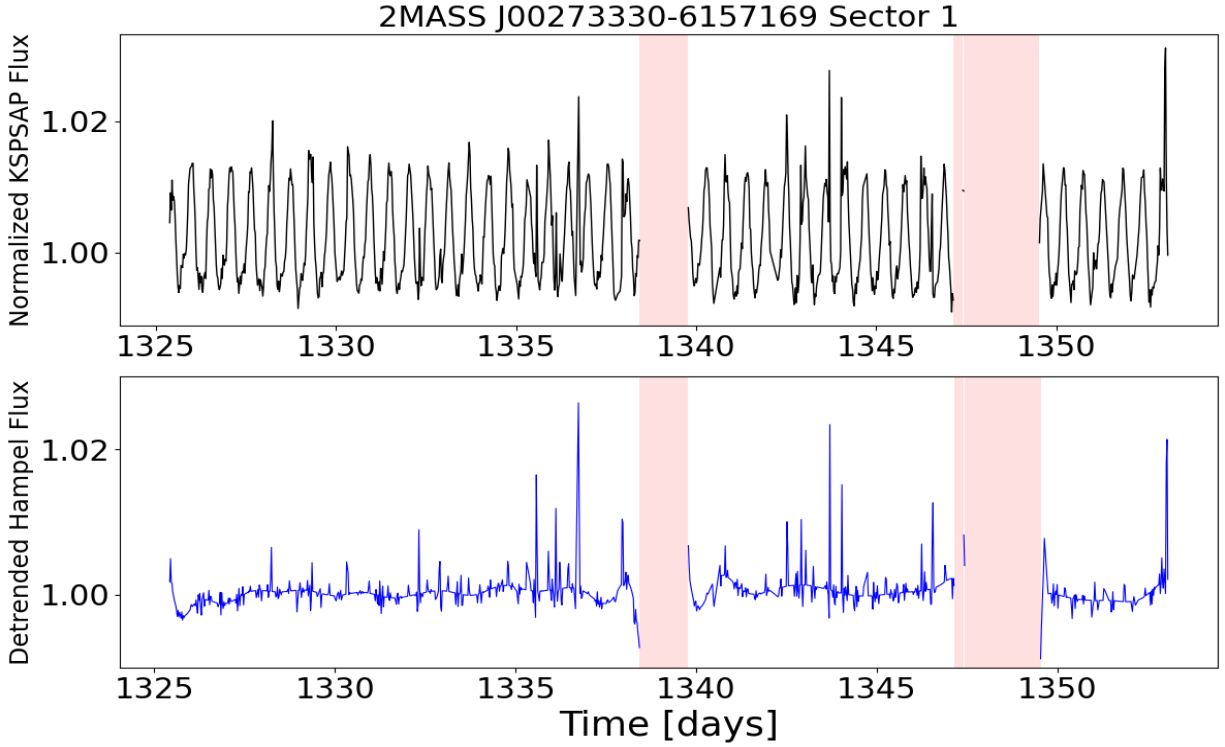


Figure 3. Top: KSPSAP detrended flux of 2MASS J00273330-6157169. A strong rotational modulation of around 0.55 days (calculated using Lomb-Scargle) is still present even after detrending. Bottom: the KSPSAP Flux with the Hampel filter applied. In both plots, the red shaded regions indicate data gaps.

absolute deviation (MAD) outlier detection to suppress impulsive outliers, before normalizing the light curve using the rolling median. This removed long-term trends while preserving flare amplitudes. A comparison between the performance of the QLP pipeline versus the Hampel filter is shown in Figure 3.

2.3. Flare Detection

The stellar flare detection process involved two major steps: identifying flare candidates and fitting these candidates to derive the relevant physical parameters.

2.3.1 Flare Candidate Identification

When a star has more than one TESS sector data, we analyzed each sector LC separately. We first identified flare candidates in each sector light curve using the 'find_flares' function from the 'AltaiPony' library (Ilin et al. 2021; Davenport 2016), which implements an algorithm to detect positive deviations in each light curve characteristic of stellar flares, which takes as input three integers N_1 , N_2 , and N_3 . The criteria for flare detection were based on the following conditions (Chang et al. 2015):

1. Positive Excursions: Candidate data points had to be positive excursions from the light curve's quiescent flux.
2. Sigma Threshold: The excursions had to be $N_1\sigma$ above the local scatter of the light curve.
3. Combined Sigma Threshold: The sum of the positive offset and calculated flux error value had to be $N_2\sigma$ above the local scatter.
4. Consecutive Points: N_3 or more consecutive data points need to satisfy the first three criteria.

We experimented with different combinations of N_1 , N_2 , and N_3 on a small subset (around 10% of the data) of the lightcurves and compared the manually confirmed flare events to determine the acceptable parameters. We set N_1 , N_2 , and N_3 to be 3, 2, and 1, respectively, to allow for appropriate candidate flare detection. This selection allowed for leniency in candidate selection due to factors such as the varying cadences in the TESS data, different signal-to-noise ratios, or different variation types in the continuum

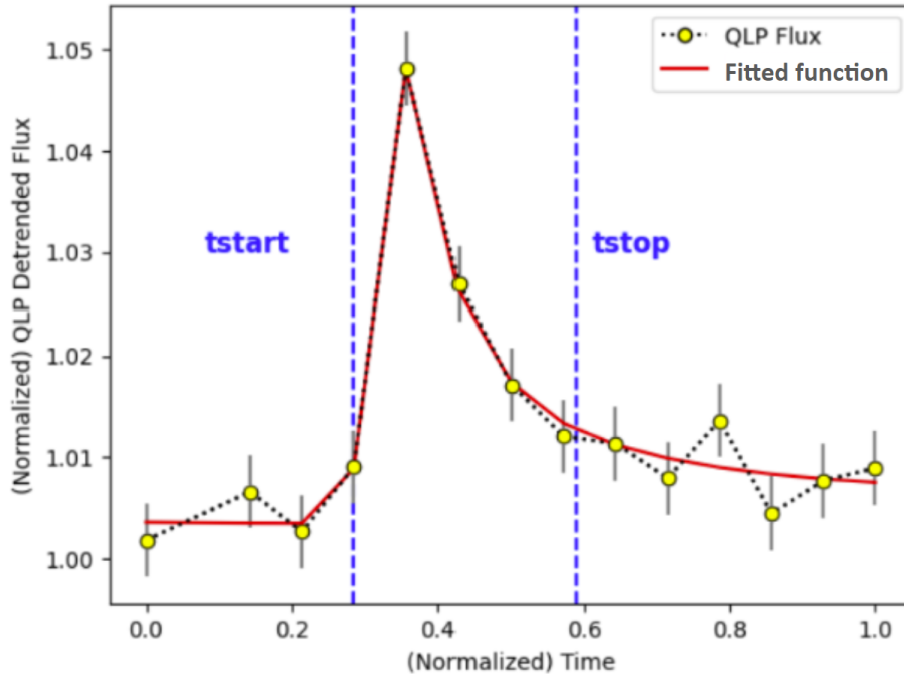


Figure 4. Example of a flare fitted using the "aflare" method, where 'tstop' is defined as 'tstart' + 'dur' from Davenport (2016), and the flare shape function takes the form of the aflare function added to a quadratic background term: $\text{aflare}(\text{time}, \text{tstart}, \text{tdur}, \text{amplitude}) + A * \text{time} ** 2 + B * \text{time} + C$

fluxes, while still imposing a limit that would mitigate the number of false positive candidates. Some flares were missing from the automatic flare detection and recovery process, which may have been due to our selection of N_1 , N_2 , and N_3 . However, if we relaxed these values by lowering each of them to '1', then it would create a number of candidate flare events (in this particular set of light curves, around 50,000 to 60,000) where only 50% of them are real.

2.3.2 Flare Fitting

Altaipony's flare candidate selection provides flare onset time (tstart), flare duration (t_dur), and flare amplitude for each flare candidate. We used these values as the initial guess and fit a function to precisely estimate flare parameters. The flare shape function mimics the behavior of stellar flares, a sharp rise in brightness followed by a slow, long decay, and we tried three different functional shapes: a Levy-Stable function, a Pulse function (Blaj et al. 2017), and Altaipony's aflare function (as shown in Figure 4 with a quadratic background term), which yielded similar fitted parameters. We decided to use Altaipony's aflare function with a quadratic background term for each flare candidate to fit tstart, t_dur, amplitude, and three coefficients for the background term. Recovered flares were defined as those with a fitted flare amplitude greater than $3\sigma_{std}$ above the quiescent flux of the light curve, where σ_{std} represents the standard deviation after performing sigma clipping on the light curve to remove outliers and reduce the influence of extreme values. The sigma clipping process iteratively excludes data points deviating by more than a set threshold (typically also 3σ) from the median flux, refining the calculation of the background noise and ensuring a more robust detection of true flare events. If the candidate flare amplitude was greater than 0.01, we sigma-clipped the entire light curve; otherwise we sigma-clipped the zoomed-in light curve region that focused on the flare. We zoomed in on the light curve region surrounding the candidate flare by selecting the time window $istart-2$ to $istart+8$. This window was used for both 30 minute and 10 minute cadence flares.

This approach allowed us to zoom in sufficiently around the flare without including excessive surrounding data. Additionally, the zoomed region was carefully checked for proximity to the edges of the light curve, adjusting the window to ensure that no indices exceeded the bounds of the data.

2.3.3 Conversion to physical units

Based on various methods in the literature, we considered a few possible approaches for converting the detected flares from raw TESS flux (in units of electron counts per second) to physical energy units. First, we converted each fitted-flare amplitude to a fractional flare energy value, by expressing the flare energy in terms of the quiescent stellar flux level (E_0).

$$E_{\text{flare}}/E_0 = f_{\text{flare}} \equiv \frac{A_{\text{flare}}}{A_{\text{q}}} \quad (2)$$

where A_{flare} is the area under the curve of the flare in the light curve (calculated by numerically integrating the light curve), and A_{q} is the area under the quiescent level of stellar flux.

The first method made use of the following relation from Ealy et al. (2024), where we first calculate the flux F_{TESS} in the TESS band, then use that value to get the energy of the flare:

$$F_{\text{TESS}} = F_0 \times 10^{-m_T/2.5} \quad (3)$$

$$ED = E_{\text{flare}}/E_0 \times (t_{\text{dur,rec}}) \times 86400 \quad (4)$$

$$E_{\text{flare}} = ED \times 4\pi d^2 \times F_{\text{TESS}} \quad (5)$$

where F_0 is zero-point flux in the TESS band ($F_0 = 4.03 \times 10^{-6}$ ergs cm^{-2} s^{-1} as derived in Sullivan et al. (2015)), m_T is the TESS band apparent magnitude, ED is the equivalent duration of the flare, $t_{\text{dur,rec}}$ is the recovered flare duration in days, and d is the Gaia distance in cm.

The second method we considered first made use of the stellar evolution model from (Baraffe et al. 2015) to estimate the bolometric luminosity of the star based on its effective temperature. Then, using the TESS bolometric correction values from Eker & Bakıř (2023) we computed the TESS band flux correction for each object, which was multiplied by the bolometric luminosity of the star, and then the equivalent duration of the flare, to get the estimated flare energy.

The third method uses the TESSreduce package produced by Ridde-Harper et al. (2021), to calibrate from TESS counts to physical flux. TESSreduce performs background subtraction, field star calibration, and applies an AB magnitude zeropoint to convert the extracted light curves into flux units (e.g., $\text{erg s}^{-1} \text{cm}^{-2}$), providing a consistent flux calibration across TESS sectors by leveraging reference stars within the cutout field. Then, using relevant distance information as well as the width of the TESS bandpass, we calculated the energy of each flare.

Each of the three methods validated and confirmed each other, giving appropriate flare energy ranges as expected based on previous studies. We hereafter use the flare energy calculation from Ridde-Harper et al. (2021) to produce the relevant figures that involve flare energy, E_{flare} .

2.4. Injection and recovery of synthetic flares

To evaluate the flare detection methodology, we performed a synthetic flare injection/recovery test. To do this, we created 30 synthetic flares in each of the QLP lightcurves considered in this study. We created synthetic flares between $\pm 10\%$ away from the beginning and ending times of the lightcurve and separated from any of the previously identified flare candidates by the average flare duration of that cadence. They were generated with random onset times, an amplitude range of 10^{-3} to 10^2 (in units of normalized flux), and a duration range of 0.0001 to 0.01 days.

The fake flare experiment, depicted in Figure 5, covered a fractional flare energy range from 10^{-4} to 10^1 . A total of 48,960 fake flares (27099 in the 30 minute cadence data and 21861 in the 10-minute cadence data) were injected into the light curves. We recovered more than 90 % of them, with $E_{\text{flare}}/E_0 \geq 10^{-3}$. These results validate the flare detection algorithms and help set the detection limits.

The analysis of fake flare recovery efficiency reveals key insights into the performance of the flare detection algorithm across different observational cadences. For both the 10-minute and 30-minute cadence data, the algorithm achieves a 90% recovery rate at a $\log_{10}(E_{\text{flare}}/E_0)$ value of approximately -2.8, and a 70% recovery rate at approximately -3.3. Below this energy threshold, the recovery rate declines further, indicating a reduction in the algorithm's ability to detect lower-energy flares effectively. The consistent increase in recovery rate with energy across both cadences further confirms the algorithm's effectiveness in identifying flares of varying intensities.

While the discrepancy in recovery rates between the 10-minute and 30-minute cadence data is near negligible, the 10-minute cadence exhibits a slightly lower 90% recovery threshold. This slight difference underscores the enhanced detection sensitivity of the 10-minute cadence, which allows for more precise and detailed flare detection. The higher time resolution in the 10-minute cadence data play a role in capturing finer details of flare activity, particularly for lower-energy flares that might be missed in the 30-minute cadence data.

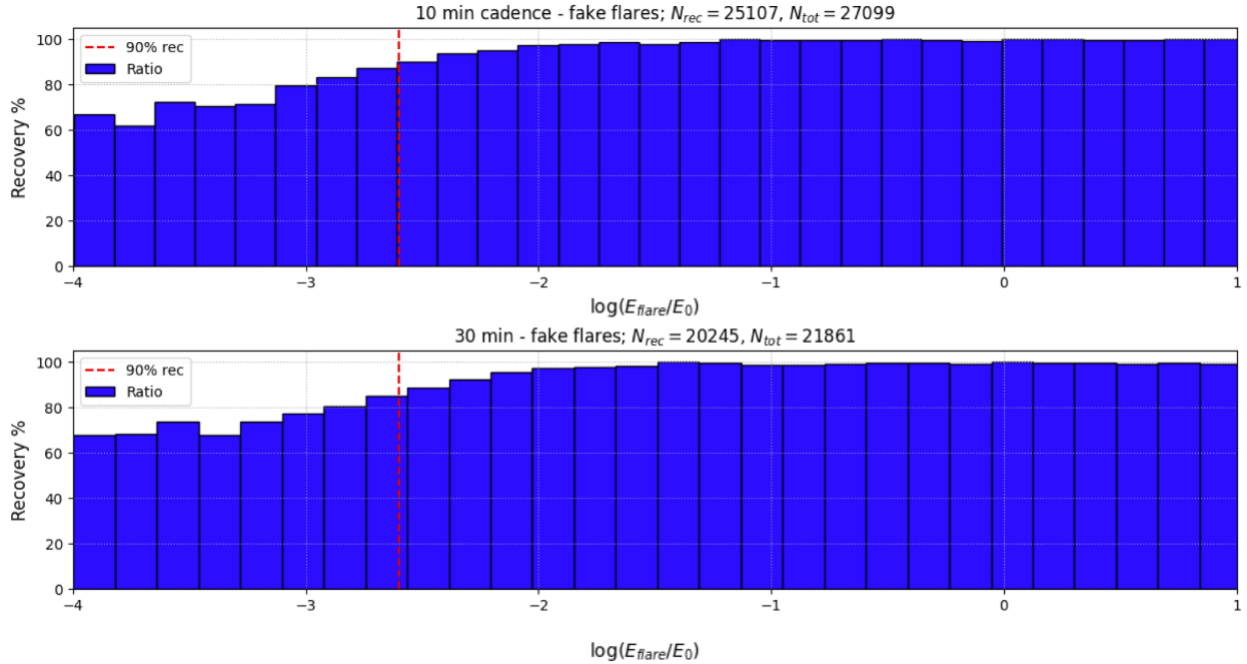


Figure 5. Recovery efficiency of fake flares as a function of flare energy ratio (E_{flare}/E_0) for both 10-minute (top) and 30-minute (bottom) cadence data. The blue bars represent the percentage of fake flares recovered at each energy level, with the total number of recovered flares N_{rec} and total number of injected flares N_{tot} indicated for each cadence set. The red dashed line marks the energy level at which the recovery efficiency reaches 90%. For both cadences, the recovery efficiency increases with flare energy, achieving over 90% recovery for flares with E_{flare}/E_0 greater than approximately $10^{-2.8}$. The higher cadence (10-minute) data shows a slightly lower energy threshold for achieving 90% recovery, highlighting the enhanced sensitivity of the 10-minute cadence data in detecting fainter flares.

Moving Group	Age (Myr)	N_{det}	$N_{poor,removed}$	$N_{edge,removed}$	$N_{noisy,removed}$	N_{rec}
TW Hydrae (TWA)	10	687	268	17	3	153
32 Orionis (Thor)	22	821	279	41	2	299
Beta Pictoris	24	2862	921	205	94	594
Columba	42	5037	1288	134	39	1144
Tucana-Horologium	45	7469	1982	333	141	2206
Argus	50	1795	836	32	13	133
Carina	60	2336	1016	61	7	487
Volans-Carina	90	781	427	13	9	109
AB Doradus	150	5628	1683	229	761	1163
Total		27416	8700	1065	1069	6288

Table 1. Summary of detected flare candidates, removed flares at each cleaning step, and final recovered flares for each moving group.

2.5. Flare Cleaning

Following the flare detection and recovery process, we implemented several cleaning procedures to remove false flare events which could have resulted from issues such as poor data quality, flares appearing near the edge of light curves, or rotational spikes within faster rotating stars being falsely classified as flare events. This was a multi-step process:

- Step 1: Flares landing on poor data quality:** we automatically removed any flares that landed on light curve data points that had a non-zero 'QUALITY' flag in the relevant FITs file column, to avoid contamination from instrumental artifacts or data gaps. In total, we removed 8700 flare candidates in this step.

2. **Step 2: Flares near the edge of the light curve:** For each flare in our sample, we first determined the associated light curve and located the flare’s onset time (t_{start}) within it. We then defined a buffer zone with a width three times the 70th percentile of all flare durations, and discarded any flare for which the time between t_{start} and either the start or end of the light curve was less than this buffer. This removed flares for which the full profile may not be captured due to edge effects. In total, we removed 1065 flare candidates in this step.
3. **Step 3: Flares from noisier light curves:** For particularly noisy light curves, we applied an additional filtering step to reject false positives due to residual systematics or high-amplitude background variation. We isolated a small time window around the candidate flare onset and extracted only those data points with ‘QUALITY’ = 0. To quantify the significance of each flare, we computed the global noise level of the light curve using sigma-clipped statistics on the detrended flux values. We then compared the recovered flare amplitude against this global noise, rejecting any candidate whose amplitude did not exceed 3 standard deviations. To avoid bias from flux spikes close to the flare, we excluded a small region around the flare peak and computed the distribution of local peak heights. In this step, we removed 1069 flare candidates.

After the above steps, we checked whether each flare candidate was at least 3σ above the quiescent flux. If the candidate met this condition, we counted it as a ‘recovered’ flare. Additionally, all subsequent analysis omit flares with a E_{flare}/E_0 value smaller than 10^{-3} , based on the results of the synthetic flares experiment. Following the above processes, we were left with 6288 stellar flares from 1272 light curves of 417 NYMG members, as shown in the last column of Table 1.

3. RESULTS

3.1. General Flare Statistics

In this section, we analyze the cumulative flare frequency distributions (FFDs) for the 9 NYMGs in Table 1, as functions of stellar age and mass, for the 6288 flares that we recovered. A subset of these flares is tabulated in Table 2.

For the FFD calculations and relevant figures that consider flare frequency, we had to consider an appropriate way to calculate the rate of flaring. We used a per-star flare rate value for these plots, first by calculating how many flares were detected for a particular star, which we called N_{flare} . We then calculate the total effective duration of observation (T_{days}) using only non-zero quality flag data points, then took $N_{\text{flare}}/T_{\text{days}}$ to get the flare rate for that star.

The analysis of flares in units of ergs, shown in Figure 6, reveals a significant difference in detection counts: 1427 flares were recovered in the 30-minute cadence data, compared to 4831 flares in the 10-minute cadence data. The smaller sample of 10-minute cadence light curves (479 LCs as opposed to 788 for 30-minute) highlights the increased sensitivity and resolution afforded by higher cadence observations, which is crucial for understanding stellar magnetic activity and its impact on stellar and planetary environments. Both FFDs show a trend consistent with the expected power law distribution of stellar flare activity.

If stellar flares are produced through a slow-driven energy dissipation system with a stationary energy input rate and a fixed threshold for triggering a flare (i.e., SOC model; Aschwanden (2019)), we can expect a power-law relationship between flare energies and frequencies. This expectation can be extended to a set of homogeneous stars with similar age, mass, rotation period, and magnetic cycle phase (i.e., a similar magnetic activity environment). However, our NYMG sample is a heterogeneous group of stars that may not share such a same magnetic activity environment. In the distributions of flares (Figures 6 - 10), we see a broader range of distributions, likely due to the mixture of flaring stars with different characteristics. Yet, we can still see the average power law behavior (of ≈ -0.6 to -0.5) from the ensemble of individual stars’ FFDs.

In Figure 7, we show the complete ensemble of individual FFDs for the full sample of detected flares in comparison to previous flare studies. We applied a Bayesian hierarchical linear regression to the ensemble of FFDs to derive a global power-law slope of the densest region of the plot. The model fits $\log_{10}\nu = \alpha\log_{10}E + \beta$, where ν is the flare rate, and E is the calculated flare energy, over the range $\log_{10}E \in [32, 34]$. Sampling with PyMC yields posterior estimates of the global slope and its credible interval, shown as the blue line in Figure 7. Outside this interval, the distribution departs from a single power law because of incompleteness at low E and small-number noise at high E . At around 10^{31} , this marks the approximate completeness boundary of our sample; below this energy, the rates should be regarded as lower limits. The fitted power law for this distribution differs from those reported in previous flare studies. Pietras et al. (2022), who analyzed flares from a larger sample of 330,000 stars from TESS, found a steeper power law index of -1.65 (in the energy range of 5×10^{33} to 10^{36} ergs), while Ealy et al. (2024) reported an index of -1.58 for a study of BPMG and AB Doradus (in the energy range of 10^{31} to 10^{35} ergs). Our findings for the complete NYMG sample yield shallower slopes than those two studies, but are closest to the power law slope found by Feinstein et al. (2024), who found a slope of -1.076 for stars with Rossby numbers lower than 0.136. Mamonova et al. (2025), who also studied several NYMGs in this age range, found a significantly steeper power law slope of -1.80 in the roughly 10^{32} to 10^{34} energy range for AU Microscopii, an active M-dwarf. Although this is one star, its slope provides a useful point of comparison

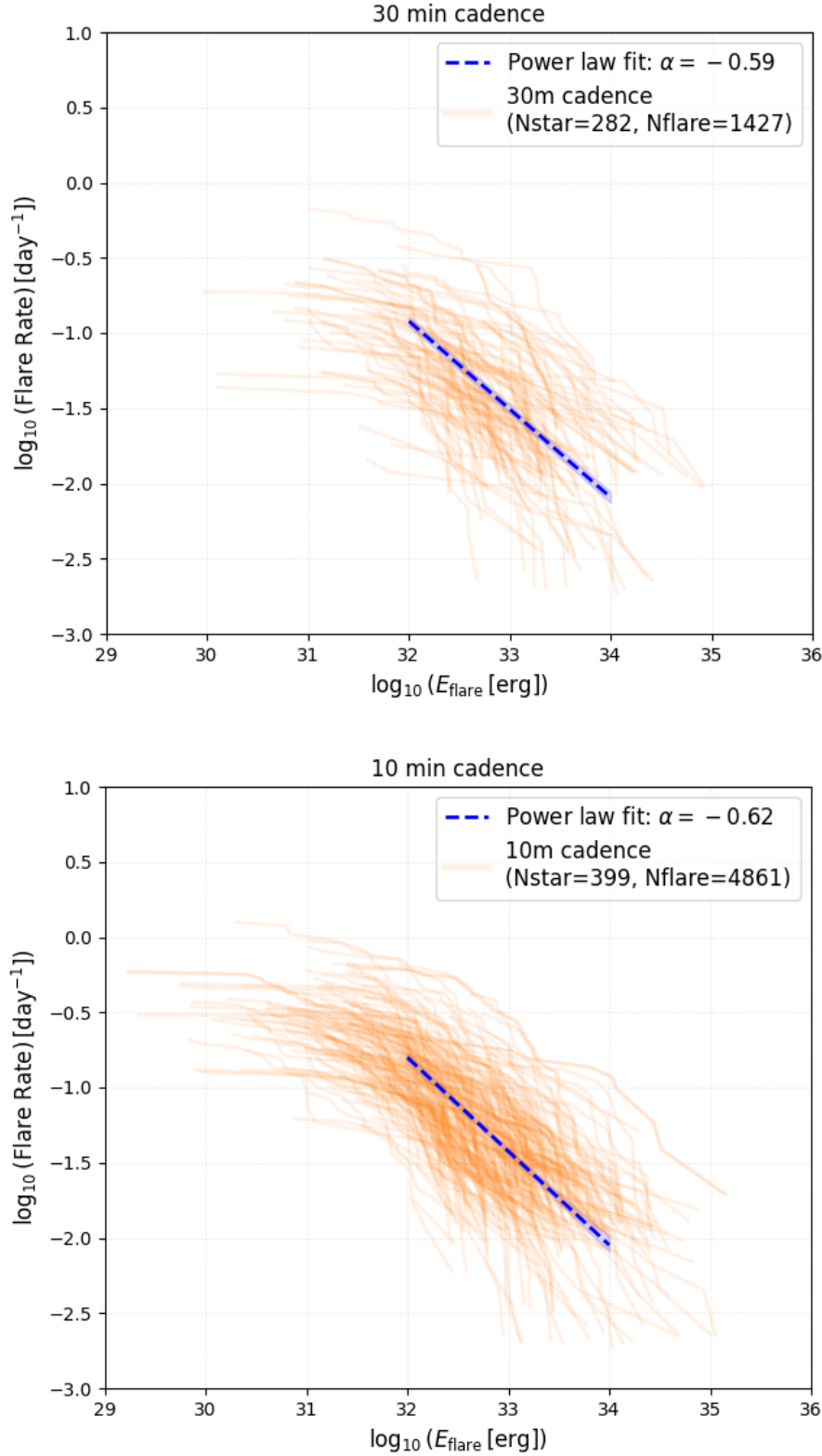


Figure 6. FFDs for flares detected in the 30-minute cadence data (top) and 10-minute cadence data (bottom). These panels include both automatically and manually detected flares. The x-axis shows the log flare energy E_{flare} in ergs, and the y-axis shows the flare rate detected at each energy level. The number of flares detected, N_{flare} , is provided in the legend for each cadence.

Member ID	Sector	Spectral Type	Moving Group	Age (Myr)	$t_{\text{start,rec}}$ (days)	$t_{\text{dur,rec}}$ (days)	ED (sec)	rec_ampl	E_{flare}/E_0	E_{flare} (ergs)
HIP25436	33	F4IV/V	Columba	42	2221.5959	0.015625	1.45	0.00500	0.0011	4.53×10^{33}
TYC.8595-1740-1	10	G5	Carina	60	1575.0757	0.012360	1.81	0.02350	0.0017	4.56×10^{32}
TYC.8595-1740-1	10	G5	Carina	60	1590.5964	0.082394	30.64	0.01338	0.0043	7.70×10^{33}
TYC.8595-1740-1	37	G5	Carina	60	2312.6378	0.007689	2.58	0.04068	0.0039	6.50×10^{32}
TYC.8595-1740-1	35	G5	Carina	60	2264.1791	0.005641	2.26	0.05121	0.0046	5.67×10^{32}
TYC.8595-1740-1	36	G5	Carina	60	2287.6448	0.004821	2.91	0.10752	0.0070	7.32×10^{32}
TYC.8595-1740-1	36	G5	Carina	60	2298.5198	0.006342	1.00	0.01793	0.0018	2.52×10^{32}
TYC.8595-1740-1	9	G5	Carina	60	1549.6172	0.008825	1.39	0.04169	0.0018	3.49×10^{32}
TYC.8595-1740-1	9	G5	Carina	60	1550.1589	0.027631	3.42	0.01073	0.0014	8.60×10^{32}
TYC.8595-1740-1	9	G5	Carina	60	1551.0131	0.009484	1.22	0.01889	0.0015	3.07×10^{32}
TYC.8595-1740-1	9	G5	Carina	60	1552.5131	0.046875	11.41	0.01257	0.0028	2.87×10^{33}
TYC.8595-1740-1	9	G5	Carina	60	1552.8464	0.008784	0.82	0.01437	0.0011	2.06×10^{32}
TYC.8574-2094-1	9	K0	Carina	60	1547.9294	0.038662	111.14	0.21192	0.033	2.77×10^{33}
TYC.8574-2094-1	9	K0	Carina	60	1559.2835	0.083225	101.13	0.04385	0.014	2.52×10^{33}
TYC.8574-2094-1	9	K0	Carina	60	1561.7001	0.110794	178.71	0.04910	0.019	4.46×10^{33}
TYC.8574-2094-1	9	K0	Carina	60	1562.5959	0.005736	1.99	0.11483	0.0040	4.97×10^{31}
TYC.8574-2094-1	9	K0	Carina	60	1563.3668	0.025215	79.06	0.35371	0.036	1.97×10^{33}
TYC.8574-2094-1	10	K0	Carina	60	1571.6375	0.033639	32.07	0.05622	0.011	8.00×10^{32}
TYC.8574-2094-1	10	K0	Carina	60	1573.1167	0.029788	26.61	0.05582	0.010	6.63×10^{32}
TYC.8574-2094-1	10	K0	Carina	60	1573.5125	0.054072	40.50	0.03944	0.0087	1.01×10^{33}
TYC.8574-2094-1	10	K0	Carina	60	1573.9292	0.009556	34.05	0.97810	0.041	8.49×10^{32}
TYC.8574-2094-1	10	K0	Carina	60	1574.9917	0.031044	15.57	0.03073	0.0058	3.88×10^{32}
TYC.8574-2094-1	10	K0	Carina	60	1575.1792	0.002885	1.01	0.03633	0.0041	2.52×10^{31}
TYC.8574-2094-1	10	K0	Carina	60	1575.4083	0.000650	0.23	0.04301	0.0042	5.85×10^{30}
TYC.8574-2094-1	10	K0	Carina	60	1577.0749	0.028143	51.35	0.19813	0.021	1.28×10^{33}
TYC.8574-2094-1	10	K0	Carina	60	1580.8666	0.008136	7.17	0.22137	0.010	1.79×10^{32}
TYC.8574-2094-1	10	K0	Carina	60	1581.6166	0.005678	24.85	1.31195	0.051	6.20×10^{32}
TYC.8574-2094-1	10	K0	Carina	60	1584.9290	0.008853	10.57	0.33566	0.014	2.64×10^{32}
TYC.8574-2094-1	10	K0	Carina	60	1587.2623	0.050705	83.25	0.08787	0.019	2.08×10^{33}
TYC.8574-2094-1	10	K0	Carina	60	1589.6164	0.010113	5.85	0.17008	0.0067	1.46×10^{32}

Table 2. Detected flare events for stars in nearby young moving groups (NYMGs). The columns represent: the member (star) identifier, TESS sector number, spectral type, moving group, $t_{\text{start,rec}}$ (recovered flare start time in BTJD days), $t_{\text{dur,rec}}$ (recovered flare duration in days), equivalent duration (ED) in seconds, rec_ampl (recovered flare amplitude), E_{flare}/E_0 (fractional flare energy), and flare energy in ergs. Values are rounded to astrophysically meaningful precision. The full table of all 6288 flares is available in machine-readable form in the online journal.

for assessing whether flare statistics in NYMGs at the population level show similar underlying scaling behavior. Additionally, at higher flare energies, the ensemble of FFDs broadly trends downward, reflecting possible variations in energy band sensitivity. The discrepancies in the power law fits could arise from the independent SOC nature of the various differing characteristics (age, mass, etc.) between each study’s individual sample of stars. These differences could also come from the varying rotation period measurements in each sample (such as the selection of fast rotators in [Feinstein et al. \(2024\)](#)), which can influence the magnetic dynamo/topology and thus the extent and overall behavior of flaring energy.

In Figures 8 - 10, we divided the stars into three mass and spectral type bins. The high-mass bin corresponds to stars with a Gaia Bp-Rp color index less than or equal to 0.8, which includes F type stars. The intermediate-mass bin encompasses stars with a Bp-Rp color index between 0.8 and 1.6, covering G-type stars and early K-type stars. Finally, the low-mass bin includes stars with a Bp-Rp color index greater than or equal to 1.6, which corresponds to late K-type and M-type stars. These bins are represented by blue, green, and red curves, respectively, in the FFD analysis plots.

As shown sequentially in Figure 8 (BPMG), Figure 9 (Tucana-Horologium), and Figure 10 (AB Doradus), there is a lack of evidence of changing flare activity behavior with respect to age. In each of these figures, the flare frequency distribution (FFD) is broken down by the Bp-Rp color index; the blue (hot) bin is sparsely populated in all three groups. For each moving group, the

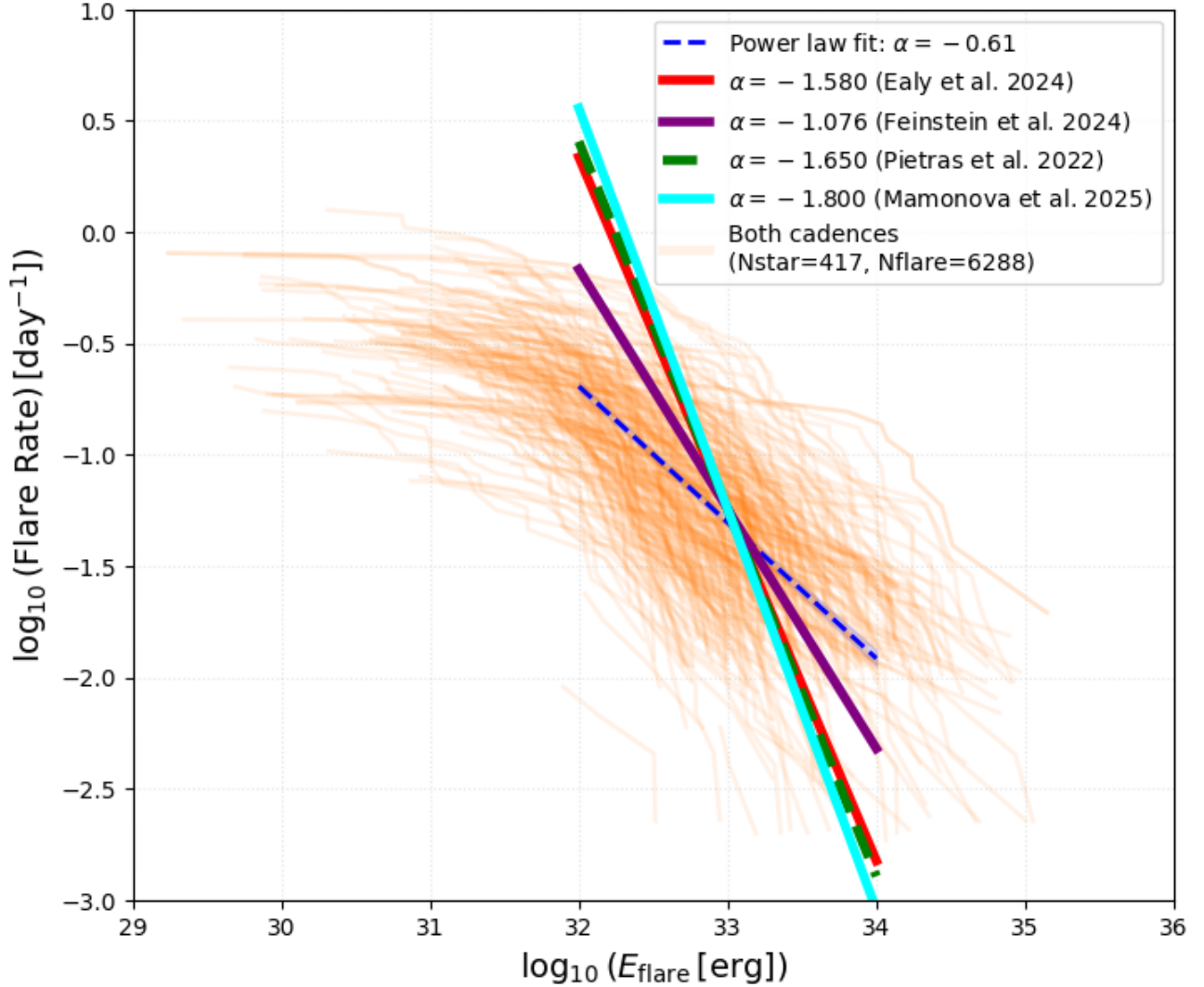


Figure 7. The flare frequency distributions (in ergs) for the entire data, with a power law fit from this work and Ealy et al. (2024), Feinstein et al. (2024), and Pietras et al. (2022)

members maintain significant flare activity across a broad energy range. Across all three moving group FFDs, cooler, late-type stars dominate the flare population, with a higher amount of flares overall for each distribution, as expected from magnetic activity scaling. There is a subtle indication of changing flare activity for solar-type stars (green points); however, this is at the mercy of small number statistics.

The Tucana-Horologium (TucHor) sample shows a broader dispersion at higher flare energies ($\log E > 33$), likely due to a larger sample of flares. This dispersion could reflect star-to-star variations within the group—differences in rotation rates, magnetic activity levels, or stellar structure—resulting in slightly different scaling behaviors between individual stars. Detection biases could also contribute, as late-type stars with lower photospheric fluxes tend to reveal weaker flares more easily.

However, in some cases, like that of AB Doradus, the scatter of flares from solar-type stars (green) is slightly higher on average. This could suggest the presence of fast rotators in solar-type stars persisting, and could also necessitate the investigation into any binaries within the sample that could lead to binary interaction effects that could also cause spin-up in stars. These factors could cause stronger magnetic activity in G-K stars. This is in line with the findings of Mamonova et al. (2025), who proposed rotation

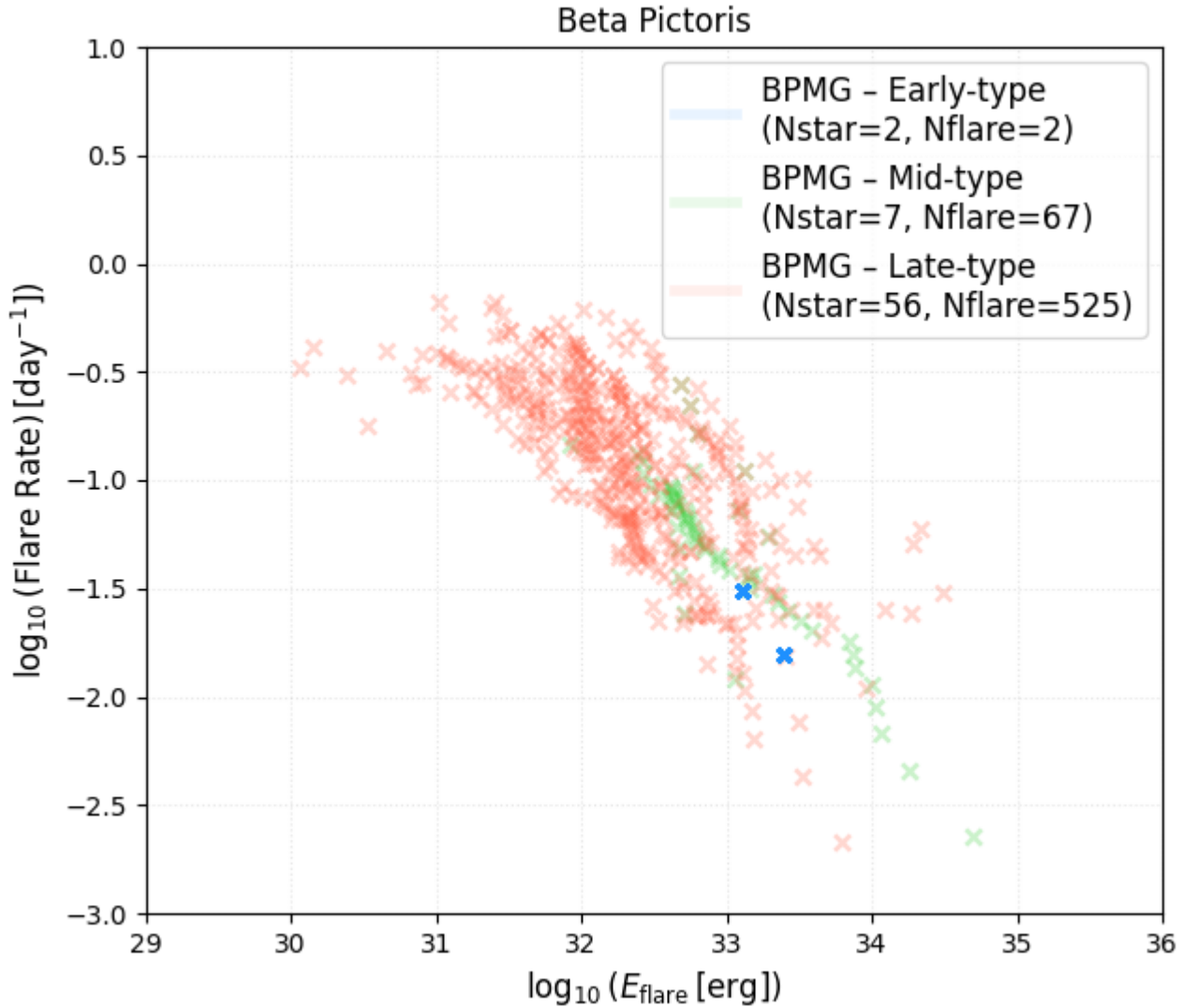


Figure 8. Flare frequency distribution (FFD) for the Beta Pictoris Moving Group (BPMG, 24 Myr), divided by Bp-Rp color index.

period as a means of gauging flare activity, as opposed to age. Nonetheless, it is consistent with previous findings that young, rapidly rotating solar-type stars are capable of producing rare, very energetic superflares (Maehara et al. 2012).

Taking a broader look at the flare activity across each moving group, we see subtle trends across later-type stars, as shown in the FFDs in Figure 11. Since this plot shows FFD curves that individually come from the same mass bin and moving group, we can assume an SOC-scaling, and thus plot the cumulative FFD curves for each sub-population, opposed to the ensemble of FFD curves for each star, as in the earlier plots. The flare rate generally stays the same as we progress in moving group age from Beta Pictoris (24 Myr) to AB Doradus (150 Myr), but at the higher energy end, the expected decrease in flaring with age is evident.

The FFDs of other moving groups are available as a figure set.

Fig. Set 10. Flare Frequency Distributions for 6 Moving Groups

In Figure 12, we show the relationship between fractional flare energy, stellar rotation period, and effective temperature. There is some noticeable vertical structure, possibly due to the binning of the rotation period values (i.e. plotting many flares that correspond to a star with a certain rotation period value). However, the distribution of flare energy appears scattered across the rotation period axis, indicating no strong correlation between flare energy and rotation period in this sample. While there is a hint of a concentration of cooler, later-type stars around a log (Rotation Period) 0.2 to 0.6 days, the scatter in the data suggests that

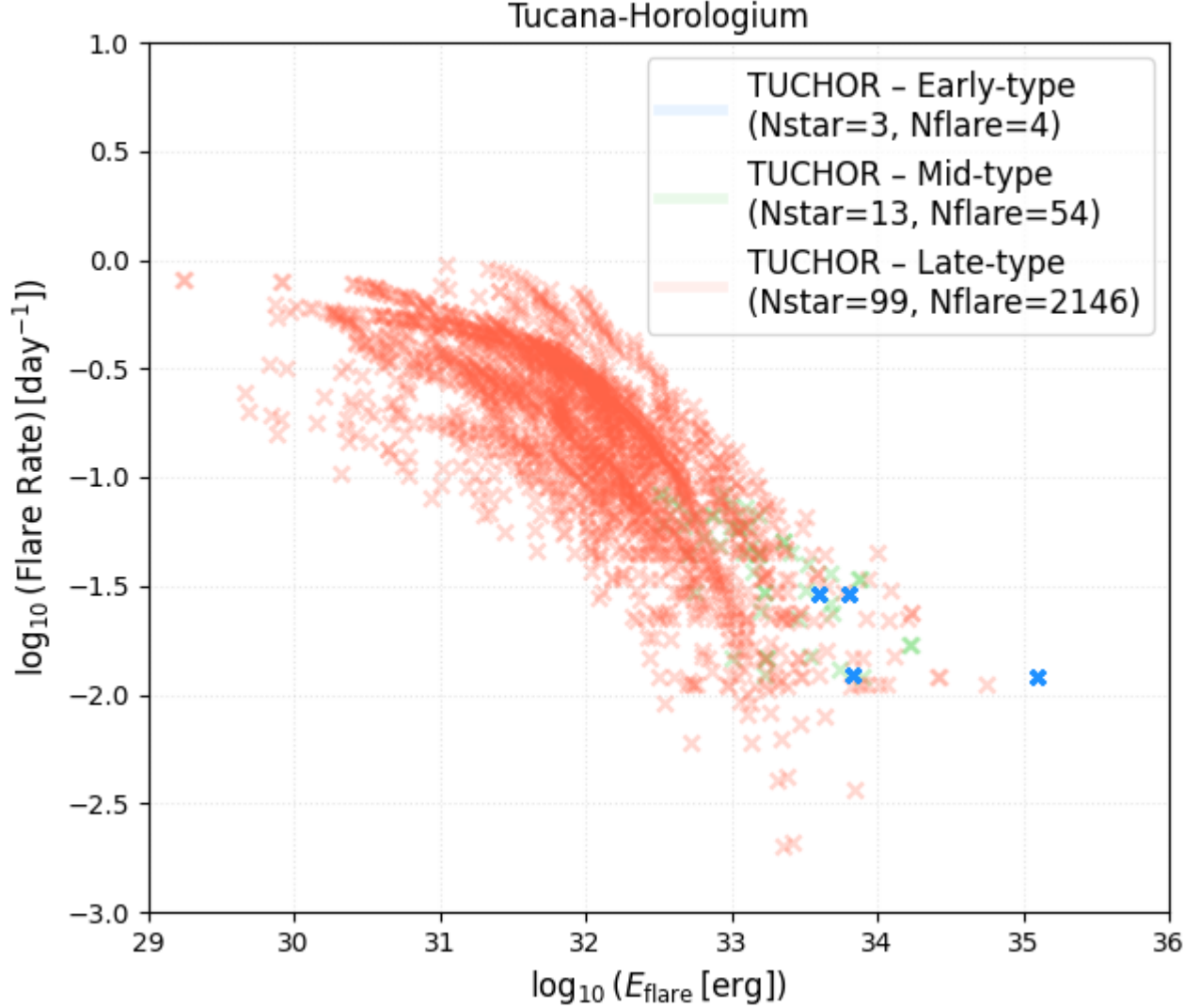


Figure 9. Flare frequency distribution (FFD) for the Tucana-Horologium Moving Group (TucHor, 45 Myr).

the relationship between flare energy and rotation is complex and likely influenced by additional stellar properties not accounted for in this analysis, or that flare activity is saturated over this age range.

The flare events span a wide energy range from approximately 10^{29} erg to 10^{36} erg and equivalent durations from 10^{-2} seconds to 10^4 seconds, as shown in Figure 13. Notably, the 10-minute cadence data detect flares with slightly shorter minimum equivalent durations compared to the 30-minute cadence. This increased sensitivity and higher resolution of the 10-minute cadence is expected, as more frequent observations enhance the capability of detecting of short-equivalent duration flares. The highest energy flares recovered in this study reach the superflare threshold as defined by Maehara et al. (2012). The strong correlation between flare energy and equivalent duration in both cadence regimes is expected, as equivalent duration is directly derived from the flare energy calculation. The observed spread in the distribution likely reflects differences in flare morphology, particularly the varying rates of flux decay in individual light curves, which influence how extended the flare appears in time.

Figure 14 shows the distribution of the average flare rate for each moving group, once again split into 3 spectral-type bins. The main distribution of flare rates are mostly within a range of just over 0.01 to 1 flares per day, as indicated by the distribution shown in Figure 15. This distribution of flare rates is consistent with previous studies like Feinstein et al. (2024) who equally analyzed young stars but up to a higher age of 300 Myr. Interestingly, there is no clear trend indicating a strong age dependence, but, as expected, cooler, redder stars exhibit higher flare rates compared to their hotter, bluer counterparts, which could be related to the convective zones and overall magnetic activity within cooler stars. However, the Argus moving group shows a higher level of

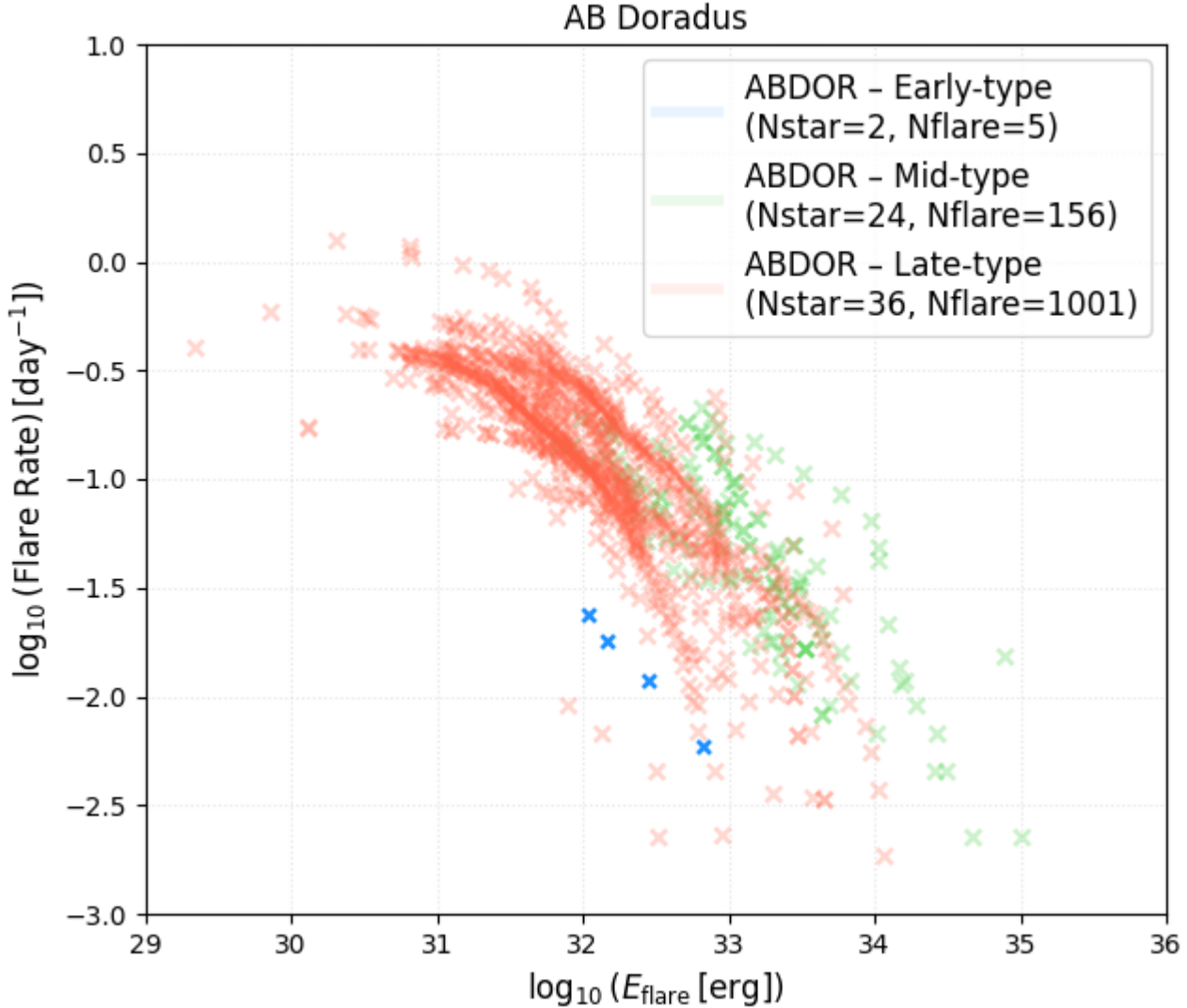


Figure 10. Flare frequency distribution (FFD) for the AB Doradus Moving Group (ABDor, 150 Myr). Flare frequency distributions for 6 additional moving groups (TucHor, ABDor, Columba, etc.) will be available in the online figure set.

flare activity in its early type members compare to its later type members which have lower flare activity, which necessitates a reevaluation of Argus in terms of age and membership. It is worth noting that in the blue bin, the flare activity is coming from a total of 18 stars across all groups, which may only partly explain the lower observed flare rates in the blue bin in general (and not just due to the general lack of flare activity in early type stars).

The lack of a connection between effective temperature and flare energy implies that other factors are likely more influential in determining the energy of stellar flares. Factors such as magnetic field strength, magnetic flux distribution, and the star’s magnetic cycle might play more crucial roles in driving flare activity. This observation is consistent with the understanding that magnetic activity, rather than temperature alone, governs the occurrence and intensity of flares. For instance, most A-type stars do not possess magnetic fields, with the exception of a few that have static fields, but do not have the capability to produce stellar flares (Braithwaite & Spruit 2004). This spectral class was relatively underrepresented in our sample, with only 26 out of 590 unique stars being A-type. This ensures that the majority of the stars we analyzed likely have magnetic fields capable of driving flares.

3.2. Higher-Energy Flare Events

We find that there are several flare events that land in the energy range of 10^{33} ergs to 10^{35} ergs from solar and late type stars. Previous studies have provided various threshold definitions of “superflares”; the seminal work of Maehara et al. (2012) used a

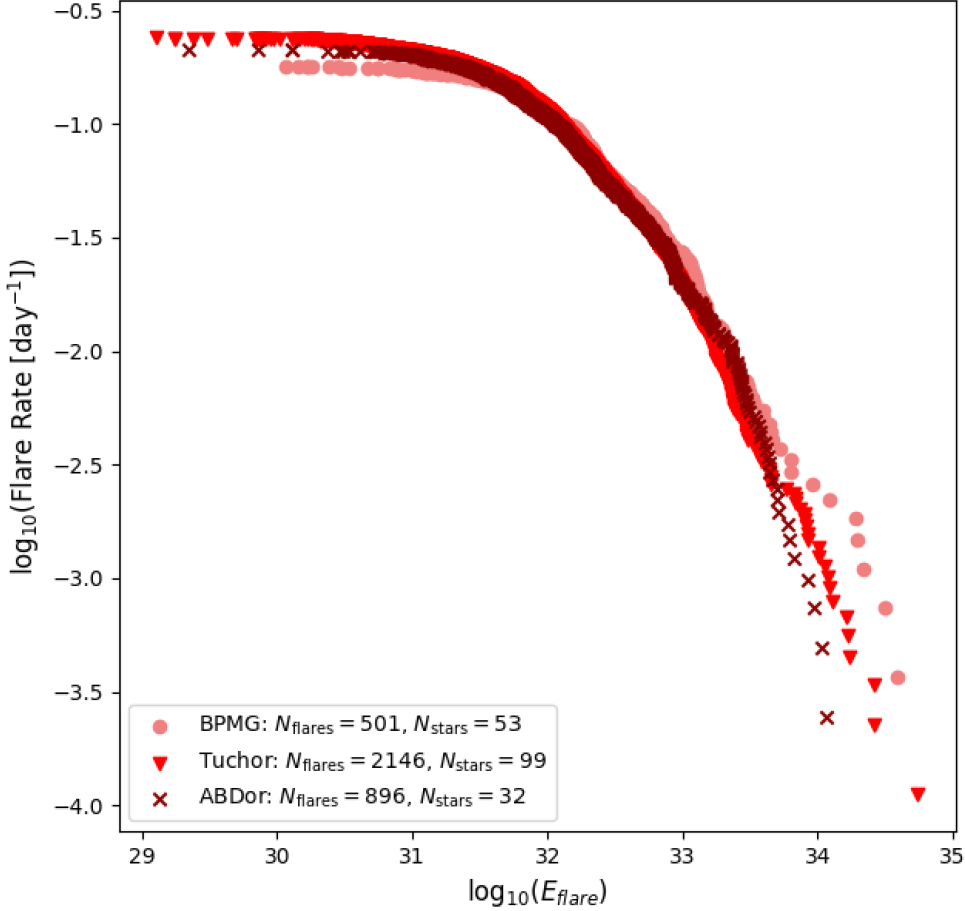


Figure 11. FFD of late type stars with respect to age for BPMG, Tuc-Hor, and AB Doradus. We assume SOC-scaling holds for this sub-sample.

threshold of 10^{33} ergs (for the analysis of solar type stars), while [Vasilyev et al. \(2024\)](#) used 10^{34} ergs as their threshold, and found that superflares occur only once per century on sun-like stars.

Since we are working with a broader range of spectral types and younger stars, we choose the threshold of 10^{34} ergs, in line with [Vasilyev et al. \(2024\)](#), in order to place an emphasis on the most extreme extraordinary “megaflare” type events. This is after accounting for stellar luminosity and spectral type scaling relations from [Zombeck \(2010\)](#), which highlight that stellar luminosity varies by several orders of magnitude from F to M type stars, making luminosity ratio L/L_{\odot} a crucial scaling factor when converting flare measurements such as equivalent duration into flare energies.

Table 3 shows a sample of the flare events above this designated threshold. Figure 11 shows that at such high energies, there is an indication that older moving groups flare less frequently than younger ones. While intermediate flare energies are more or less consistent across all three moving groups, the highest energy flares show a clear evolution. At lower energies beyond the detection limit of $\log E \approx 31$, the difference cannot be justified, and has to be taken cautiously.

If we concentrate on the tail end of each distribution, we see that in the megaflaring energy range, the median flare rate is around $10^{-3.5}$, or roughly 0.0003 flares per day. Extrapolating from this value, we can make the assumption that flares of this caliber occur around 11 times per century on late-type stars (about 10 times higher than older, sun-like stars; see [Vasilyev et al. \(2024\)](#)). For M-dwarf hosts, repeated flaring at this scale may erode planetary atmospheres ([do Amaral et al. 2025](#)), while for solar-type stars, rare but extreme superflares could intermittently alter the radiation environment of surrounding planets.

4. SUMMARY AND DISCUSSION

In this work, we performed a comprehensive analysis of stellar flares in members of Nearby Young Moving Groups (NYMGs) aged 10-150 Myr using photometric data from the Transiting Exoplanet Survey Satellite (TESS). Our study focused on charac-

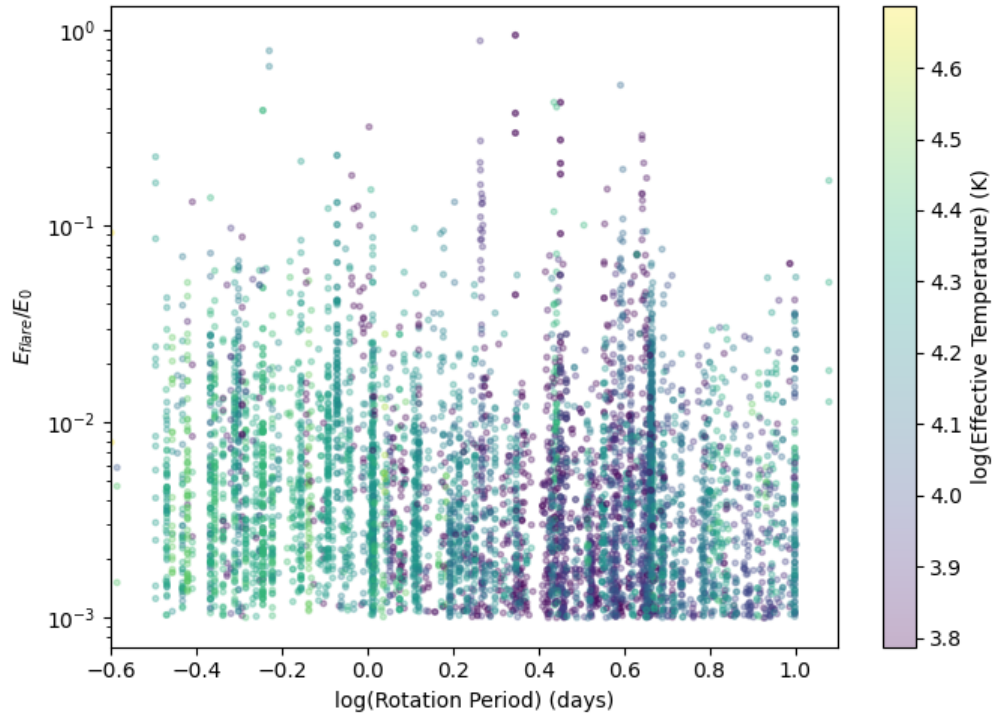


Figure 12. Fractional flare energy (E_{flare}/E_0) plotted with respect to rotation period and temperature.

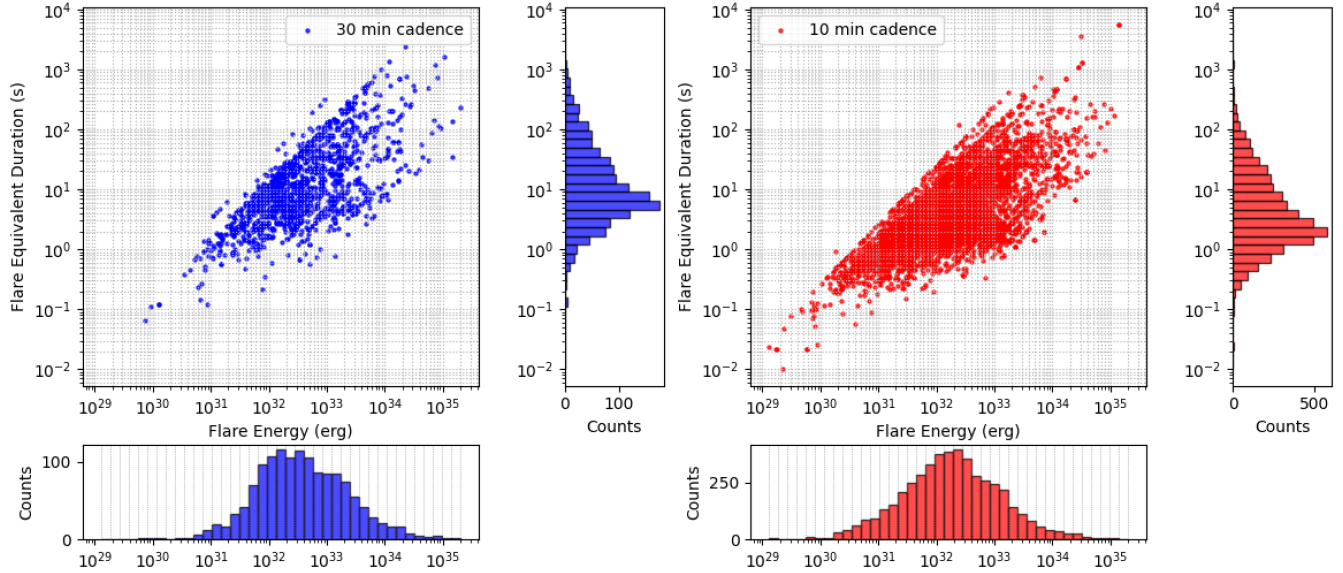


Figure 13. Scatter plot showing the relationship between flare energy (in erg) and flare duration (in days) for 30-minute cadence data (left, blue) and 10-minute cadence data (right, red). The data reveal a positive correlation between flare energy and duration, consistent with models of stellar flare activity. The higher cadence (10-minute) data shows a broader range of detected flare energies and durations, including slightly more short-duration flares, indicating enhanced sensitivity to both low-energy short-duration and high-energy long-duration flares.

terizing the flare frequency distributions (FFDs) and investigating the relationship between stellar flares and physical parameters like age, spectral type, rotation period, and effective temperature.

Our analysis yielded several important results:

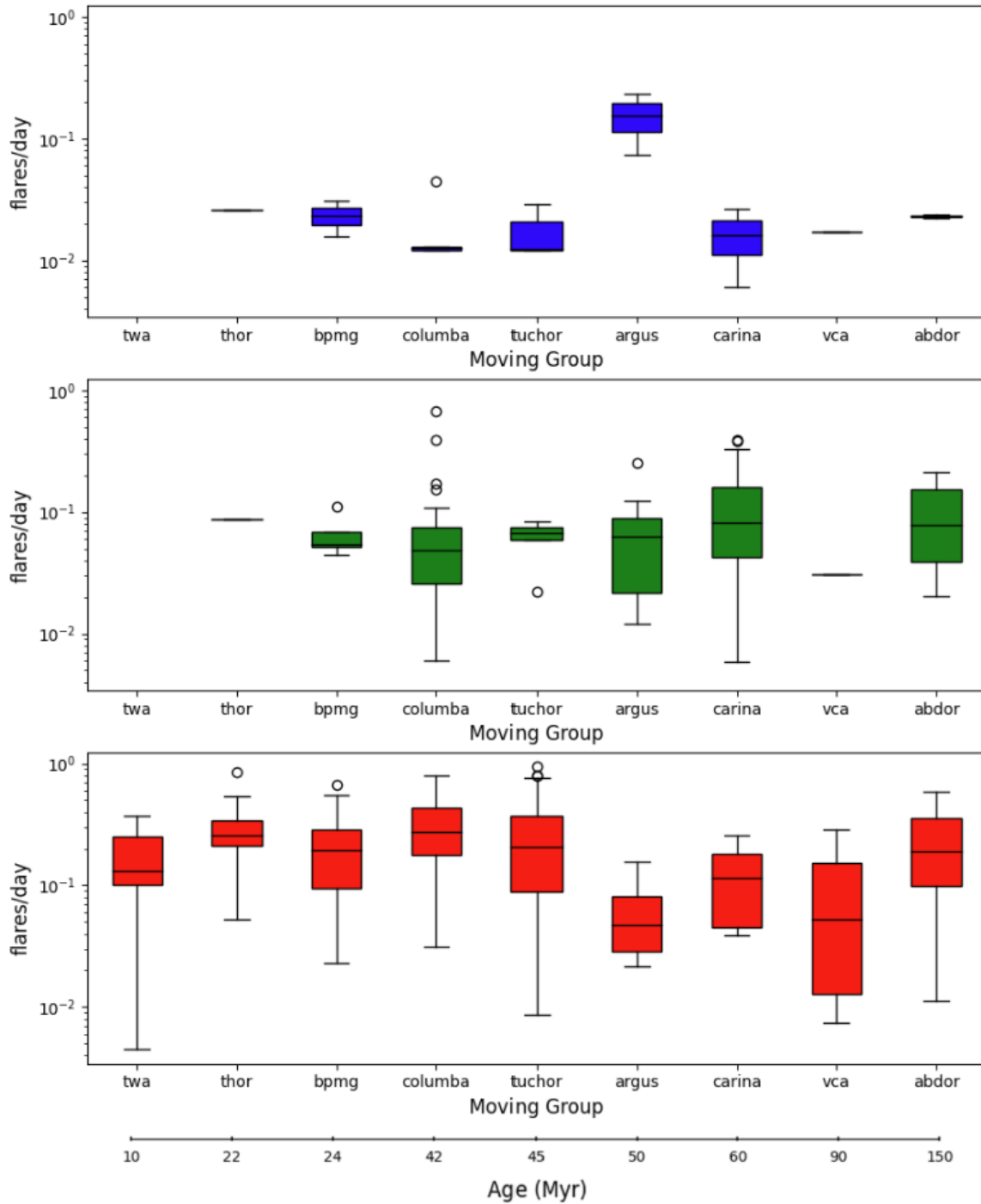


Figure 14. Average flare rate (number of flares per day per star) for members of different young moving groups (MGs), categorized by spectral type. The panels display average flare rates for stars of different Gaia BP-RP color indices, indicating their spectral types: *Top*: stars with a Gaia BP-RP color index less than or equal to 0.75, covering A and F spectral types. The total number of stars in this bin is 18. *Middle*: stars with a Gaia BP-RP color index between 0.75 and 1.8, corresponding to G-type stars and early K-type stars. The total number of stars in this bin is 89. *Bottom*: stars with a Gaia BP-RP color index greater than or equal to 1.8, representing late K-type and M-type stars. The late-type stars show an average flare rate roughly 5-6 times higher than early type stars. The total number of stars in this bin is 310.

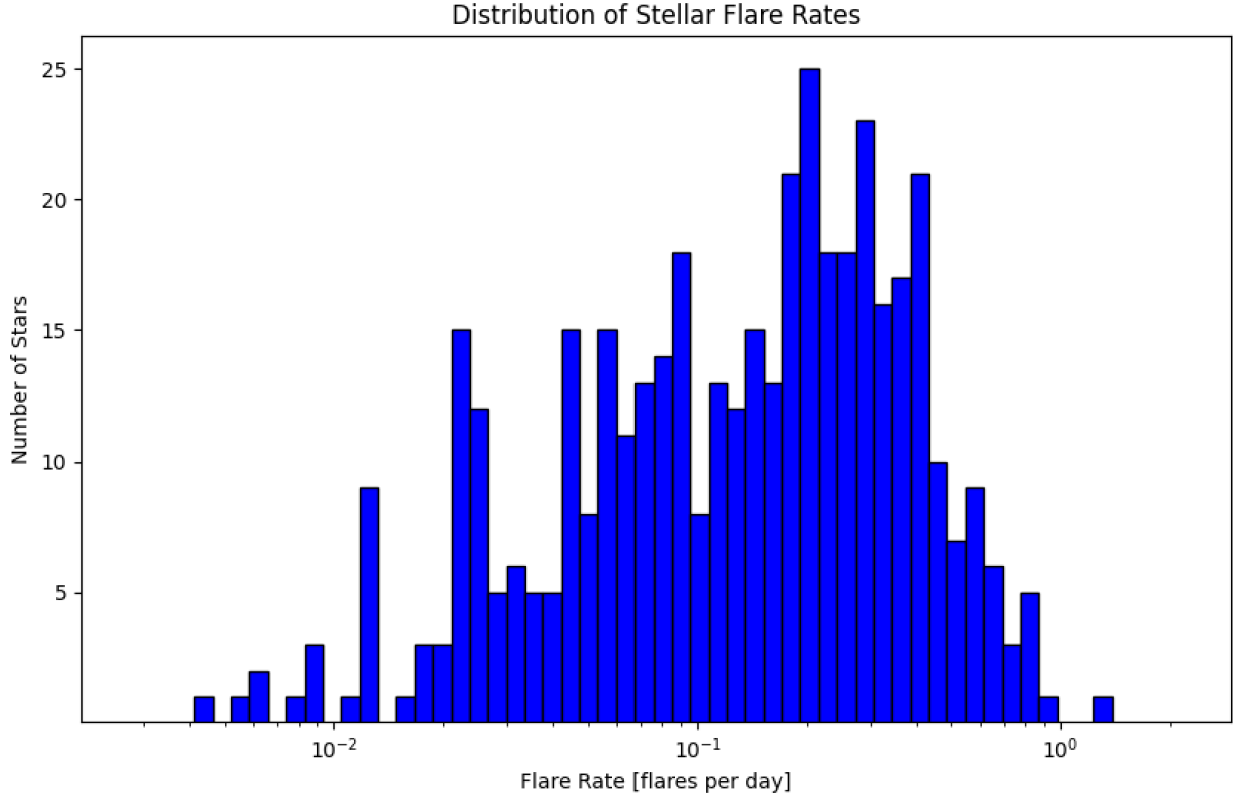


Figure 15. Distribution of flare rate (in units of flares/day) for the flaring stars in the NYMG sample.

1. **Ubiquity of Flares:** All NYMG stars with available TESS QLP light curves analyzed in this work exhibit one or more stellar flares, confirming that flare activity is nearly universal among young stars within the 10–150 Myr age range.
2. **Flare Detection:** Using our flare identification scheme, we could identify 6288 flares from 417 stars at a 90% detection rate above E_{flare}/E_0 values of 10^{-3} .
3. **Age Dependence:** No clear age dependence of flare activity is observed across the ~ 10 –150 Myr range for any spectral type. Over this age range, there may be saturated flare activity, similar to the case of X-ray emission on low-mass stars.
4. **Spectral-Type Dependence:** Lower-mass stars (M-type) display flare frequencies approximately 5–6 times higher than those of G–K type stars, and roughly an order of magnitude higher than F-type stars. This behavior is consistent with enhanced magnetic activity in low mass stars.
5. **Flare Rates:** NYMG members show average flare rates exceeding 0.01 flares per day over the energy range of 10^{31} – 10^{33} erg. More energetic events ($E > 10^{34}$ erg) occur less frequently, roughly once every few years.
6. **Cadence Dependence:** The 10-minute cadence data yield approximately 5.5 times more flares than the 30-minute cadence data over the same energy range. This increase is attributed to the improved temporal sampling of flare peaks at higher cadence. Extrapolating from this result, we expect the 200-second TESS cadence mode to achieve an additional factor of ~ 2 –3 higher flare recovery efficiency.
7. **Superflare Fraction:** Based on the adopted threshold of superflares from [Vasilyev et al. \(2024\)](#) ($E \geq 10^{34}$ erg), approximately 25% of NYMG members display superflare activity. When the superflare threshold is scaled to the quiescent flux level as a function of spectral type, about 10% of NYMG members still exhibit superflares.
8. **Flare Frequency Distribution (FFD) Slope:** The power-law index of the FFDs, derived from a fit over the 10^{32} – 10^{34} erg range, is $\alpha = -0.51$, which is shallower than values reported in previous studies ($-1.1 \lesssim \alpha \lesssim -1.7$; e.g., [Pietras et al.](#)

Member ID	Sector	Spectral Type	Moving Group	Age (Myr)	$t_{\text{start,rec}}$ (days)	$t_{\text{dur,rec}}$ (days)	ED (sec)	rec_amp1	E_{flare}/E_0	E_{flare} (ergs)
PMM_4809	36	G3e	Argus	50	2285.3185	0.02910	38.35	0.0491	0.015	3.79×10^{34}
HD_12894	3	F2V	Tuc-Hor	45	1387.2847	0.06507	34.52	0.0221	0.0061	1.37×10^{35}
TYC_8595-1740-1	37	G5	Carina	60	2318.6933	0.05625	77.00	0.0328	0.016	1.94×10^{34}
TYC_8595-1740-1	37	G5	Carina	60	2321.5544	0.05625	41.17	0.0175	0.0085	1.03×10^{34}
TYC_8595-1740-1	37	G5	Carina	60	2324.2002	0.05625	51.03	0.0217	0.011	1.28×10^{34}
TYC_8595-1740-1	35	G5	Carina	60	2263.4986	0.03774	162.92	0.1334	0.050	4.10×10^{34}
TYC_8595-1740-1	36	G5	Carina	60	2287.0128	0.05625	60.43	0.0257	0.012	1.52×10^{34}
TYC_8595-1740-1	36	G5	Carina	60	2296.2906	0.05563	66.14	0.0285	0.014	1.66×10^{34}
TYC_8595-1740-1	36	G5	Carina	60	2299.5684	0.03262	65.79	0.0691	0.023	1.65×10^{34}
TYC_8595-1740-1	36	G5	Carina	60	2303.8809	0.01421	42.92	0.1887	0.035	1.08×10^{34}
TYC_8595-1740-1	9	G5	Carina	60	1550.6589	0.10543	42.11	0.0122	0.0046	1.06×10^{34}
2MASS_J09345645-64595	37	F5V	VCA	90	2317.5683	0.01610	6.64	0.0248	0.0048	2.37×10^{34}
HD_302321	10	F8	Carina	60	1590.9509	0.02136	6.61	0.0400	0.0036	1.08×10^{34}
HD_85151B	9	G9V	Argus	50	1564.3060	0.12744	708.23	0.1551	0.064	1.70×10^{34}
HD_85151B	36	G9V	Argus	50	2288.1460	0.04317	687.36	0.4497	0.18	1.65×10^{34}
HD_85151B	36	G9V	Argus	50	2290.4099	0.01990	472.73	1.0297	0.27	1.14×10^{34}
HD_85151B	36	G9V	Argus	50	2301.8959	0.02983	1101.90	1.3509	0.43	2.65×10^{34}
HD_85151B	35	G9V	Argus	50	2263.2499	0.05625	4582.36	1.9512	0.94	1.10×10^{35}
HD_85151B	35	G9V	Argus	50	2275.0140	0.04132	1066.33	0.7340	0.30	2.56×10^{34}

Table 3. The first 20 flares in the dataset above the designated threshold of 10^{34} ergs. The columns represent: the member (star) identifier, TESS sector number, spectral type, moving group, $t_{\text{start,rec}}$ (recovered flare start time in BTJD days), $t_{\text{dur,rec}}$ (recovered flare duration in days), equivalent duration (ED) in seconds, rec_amp1 (recovered flare amplitude), E_{flare}/E_0 (fractional flare energy), and flare energy in ergs. Values are rounded to astrophysically meaningful precision. The full table of all 183 high energy flare events is available in machine-readable form in the online journal.

(2022); Feinstein et al. (2024)). This difference likely arises from the inclusion of a larger number of low-energy flares, which flatten the observed slope.

9. **Rate of Flaring:** While no clear trend in overall flare rates with age is seen, early-type stars exhibit lower mean flare rates (~ 0.1 flares/day) compared to mid- and late-type stars (~ 0.3 – 0.6 flares/day). The overall flare rate distribution remains consistent across the NYMGs, suggesting stable magnetic activity during this epoch.

10. **Argus Moving Group Anomaly:** In the Argus Moving Group, early-type stars show unusually elevated flare activity levels (by $\geq 3\sigma$ or several times higher than similar stars in other groups), while M-type members display comparatively weaker flare activity. These discrepancies suggest that the Argus group’s age and/or membership assignments should be revisited through detailed spectroscopic and kinematic analyses.

Future work should focus on expanding the sample size to include older stellar populations from open clusters (such as the Hyades cluster or Ursa Major Association), field stars, more intermediate and high-mass stars, as well as exploring the long-term activity cycles of NYMG members, using the abundance of TESS data from the past 7 years. Additionally, further analysis of flare activity in different observational cadences (such as Cycle 5 and later from TESS) will enhance our understanding of magnetic field evolution in young stars, as the larger sample of stars and enhanced temporal resolution will equally allow for the increased number of high energy, superflare events as well as the detection of previously missed lower energy flares, respectively. Finally, the flare statistics we collected for young stars may allow us to use them as a proxy for assessing stellar habitability.

¹ The authors would like to thank the anonymous referees for the comments that improved the quality of this paper. This research
² was supported by NASA Grant Number 80NSSC25K7805. We acknowledge the use of data from the Transiting Exoplanet Survey
³ Satellite (TESS) mission (TESS Team 2018), a NASA Explorer mission led and operated by MIT, and funded by NASA’s Science
⁴ Mission Directorate. We thank the TESS team for making this data publicly available and accessible.

Facilities: TESS

Software: astropy (Astropy Collaboration et al. 2013, 2018), Cloudy (Ferland et al. 2013), Source Extractor (Bertin & Arnouts 1996), altaipony (Ilin et al. 2021; Davenport 2016), lightkurve (Lightkurve Collaboration et al. 2018)

REFERENCES

- Aschwanden, M. J. 2019, *The Astrophysical Journal*, 880, 105, doi: [10.3847/1538-4357/ab29f4](https://doi.org/10.3847/1538-4357/ab29f4)
- Astropy Collaboration, Robitaille, T. P., Tollerud, E. J., et al. 2013, *A&A*, 558, A33, doi: [10.1051/0004-6361/201322068](https://doi.org/10.1051/0004-6361/201322068)
- Astropy Collaboration, Price-Whelan, A. M., Sipőcz, B. M., et al. 2018, *AJ*, 156, 123, doi: [10.3847/1538-3881/aabc4f](https://doi.org/10.3847/1538-3881/aabc4f)
- Baraffe, I., Homeier, D., Allard, F., & Chabrier, G. 2015, *A&A*, 577, A42, doi: [10.1051/0004-6361/201425481](https://doi.org/10.1051/0004-6361/201425481)
- Barrado y Navascués, D., Stauffer, J. R., Song, I., & Caillault, J. P. 1999, *ApJL*, 520, L123, doi: [10.1086/312162](https://doi.org/10.1086/312162)
- Bertin, E., & Arnouts, S. 1996, *A&AS*, 117, 393, doi: [10.1051/aas:1996164](https://doi.org/10.1051/aas:1996164)
- Braithwaite, J., & Spruit, H. C. 2004, *Nature*, 431, 819, doi: [10.1038/nature02934](https://doi.org/10.1038/nature02934)
- Caldiroli, A., Haardt, F., Gallo, E., et al. 2025, arXiv e-prints, arXiv:2506.08014, doi: [10.48550/arXiv.2506.08014](https://doi.org/10.48550/arXiv.2506.08014)
- Chang, S. W., Byun, Y. I., & Hartman, J. D. 2015, *ApJ*, 814, 35, doi: [10.1088/0004-637X/814/1/35](https://doi.org/10.1088/0004-637X/814/1/35)
- Crowley, J., Wheatland, M. S., & Yang, K. 2022, *ApJ*, 941, 193, doi: [10.3847/1538-4357/aca476](https://doi.org/10.3847/1538-4357/aca476)
- Davenport, J. R. A. 2016, *The Astrophysical Journal*, 829, 23, doi: [10.3847/0004-637X/829/1/23](https://doi.org/10.3847/0004-637X/829/1/23)
- Davenport, J. R. A., Covey, K. R., Clarke, R. W., et al. 2019, *ApJ*, 871, 241, doi: [10.3847/1538-4357/aafb76](https://doi.org/10.3847/1538-4357/aafb76)
- do Amaral, L. N. R., Shkolnik, E. L., Loyd, R. O. P., & Peacock, S. 2025, *The Astrophysical Journal*, 985, 100, doi: [10.3847/1538-4357/adc932](https://doi.org/10.3847/1538-4357/adc932)
- Dressing, C. D., & Charbonneau, D. 2013, *ApJ*, 767, 95, doi: [10.1088/0004-637X/767/1/95](https://doi.org/10.1088/0004-637X/767/1/95)
- Ealy, J. N., Schlieder, J. E., Komacek, T. D., & Gilbert, E. A. 2024, *AJ*, 168, 173, doi: [10.3847/1538-3881/ad6b7e](https://doi.org/10.3847/1538-3881/ad6b7e)
- Eker, Z., & Bakış, V. 2023, *Monthly Notices of the Royal Astronomical Society*, 523, 2440–2452, doi: [10.1093/mnras/stad1563](https://doi.org/10.1093/mnras/stad1563)
- Feinstein, A. D., Montet, B. T., Ansdell, M., et al. 2020, *The Astronomical Journal*, 160, 219, doi: [10.3847/1538-3881/abac0a](https://doi.org/10.3847/1538-3881/abac0a)
- Feinstein, A. D., Seligman, D. Z., France, K., Gagné, J., & Kowalski, A. 2024, Evolution of Flare Activity in GKM Stars Younger than 300 Myr over Five Years of TESS Observations. <https://arxiv.org/abs/2405.00850>
- Ferland, G. J., Porter, R. L., van Hoof, P. A. M., et al. 2013, *RMxAA*, 49, 137. <https://arxiv.org/abs/1302.4485>
- Gagné, J., Faherty, J. K., Mamajek, E. E., et al. 2017, *The Astrophysical Journal Supplement Series*, 228, 18, doi: [10.3847/1538-4365/228/2/18](https://doi.org/10.3847/1538-4365/228/2/18)
- Hazra, G., Vidotto, A. A., Carolan, S., D’Angelo, C. V., & Manchester, W. 2021, *Monthly Notices of the Royal Astronomical Society*, 509, 5858, doi: [10.1093/mnras/stab3271](https://doi.org/10.1093/mnras/stab3271)
- Henry, T. J., Jao, W.-C., Subasavage, J. P., et al. 2006, *AJ*, 132, 2360, doi: [10.1086/508233](https://doi.org/10.1086/508233)
- Howard, W. S., & Law, N. M. 2021, *The Astrophysical Journal*, 920, 42, doi: [10.3847/1538-4357/ac142a](https://doi.org/10.3847/1538-4357/ac142a)
- Ilin, E., Schmidt, S. J., Poppenhäger, K., et al. 2021, *A&A*, 645, A42, doi: [10.1051/0004-6361/202039198](https://doi.org/10.1051/0004-6361/202039198)
- Lee, J., & Song, I. 2019, *MNRAS*, 489, 2189, doi: [10.1093/mnras/stz2290](https://doi.org/10.1093/mnras/stz2290)
- Lee, J., Song, I., & Murphy, S. J. 2022, *Monthly Notices of the Royal Astronomical Society*, 511, 6179, doi: [10.1093/mnras/stac358](https://doi.org/10.1093/mnras/stac358)
- Lightkurve Collaboration, Cardoso, J. V. d. M., Hedges, C., et al. 2018, *Lightkurve: Kepler and TESS time series analysis in Python*, *Astrophysics Source Code Library*. <http://ascl.net/1812.013>
- Macintosh, B., Graham, J. R., Barman, T., et al. 2015, *Science*, 350, 64, doi: [10.1126/science.aac5891](https://doi.org/10.1126/science.aac5891)
- Maehara, H., Shibayama, T., Notsu, S., et al. 2012, *Nature*, 485, 478, doi: [10.1038/nature11063](https://doi.org/10.1038/nature11063)
- Mamonova, E., Shan, Y., Kowalski, A. F., Wedemeyer, S., & Werner, S. C. 2025, *Astronomy I&A: Astrophysics*, 700, A53, doi: [10.1051/0004-6361/202554614](https://doi.org/10.1051/0004-6361/202554614)
- Marley, M. S., Fortney, J. J., Hubickyj, O., Bodenheimer, P., & Lissauer, J. J. 2007, *ApJ*, 655, 541, doi: [10.1086/509759](https://doi.org/10.1086/509759)
- Murray, C. A., Queloz, D., Gillon, M., et al. 2022, *Monthly Notices of the Royal Astronomical Society*, 513, 2615, doi: [10.1093/mnras/stac1078](https://doi.org/10.1093/mnras/stac1078)
- Paudel, R. R., Barclay, T., Youngblood, A., et al. 2024, A Multiwavelength Survey of Nearby M dwarfs: Optical and Near-Ultraviolet Flares and Activity with Contemporaneous TESS, Kepler/K2, *Swift*, and HST Observations. <https://arxiv.org/abs/2404.12310>
- Pietras, M., Falewicz, R., Siarkowski, M., Bicz, K., & Preś, P. 2022, *ApJ*, 935, 143, doi: [10.3847/1538-4357/ac8352](https://doi.org/10.3847/1538-4357/ac8352)
- Rebull, L. M., Stauffer, J. R., Hillenbrand, L. A., et al. 2022, *The Astronomical Journal*, 164, 80, doi: [10.3847/1538-3881/ac75f1](https://doi.org/10.3847/1538-3881/ac75f1)

- Ricker, G. R., Winn, J. N., Vanderspek, R., et al. 2014, in Society of Photo-Optical Instrumentation Engineers (SPIE) Conference Series, Vol. 9143, Space Telescopes and Instrumentation 2014: Optical, Infrared, and Millimeter Wave, ed. J. Oschmann, Jacobus M., M. Clampin, G. G. Fazio, & H. A. MacEwen, 914320, doi: [10.1117/12.2063489](https://doi.org/10.1117/12.2063489)
- Ridden-Harper, R., Rest, A., Hounsell, R., et al. 2021, arXiv e-prints, arXiv:2111.15006. <https://arxiv.org/abs/2111.15006>
- Spiegel, D. S., & Burrows, A. 2012, ApJ, 745, 174, doi: [10.1088/0004-637X/745/2/174](https://doi.org/10.1088/0004-637X/745/2/174)
- Sullivan, P. W., Winn, J. N., Berta-Thompson, Z. K., et al. 2015, The Astrophysical Journal, 809, 77, doi: [10.1088/0004-637X/809/1/77](https://doi.org/10.1088/0004-637X/809/1/77)
- TESS Team. 2018, TESS Input Catalog and Candidate Target List, STScI/MAST, doi: [10.17909/FWDT-2X66](https://doi.org/10.17909/FWDT-2X66)
- Torres, G., Winn, J. N., & Holman, M. J. 2008, ApJ, 677, 1324, doi: [10.1086/529429](https://doi.org/10.1086/529429)
- Vasilyev, V., Reinhold, T., Shapiro, A., et al. 2024, Science (New York, N.Y.), 386, 1301, doi: [10.1126/science.adl5441](https://doi.org/10.1126/science.adl5441)
- Verbeeck, C., Kraaikamp, E., Ryan, D. F., & Podladchikova, O. 2019, The Astrophysical Journal, 884, 50, doi: [10.3847/1538-4357/ab3425](https://doi.org/10.3847/1538-4357/ab3425)
- Zombeck, M. 2010, Handbook of Space Astronomy and Astrophysics (Martin Zombeck). <https://books.google.com/books?id=F22kkgAACAAJ>
- Zuckerman, B., Rhee, J. H., Song, I., & Bessell, M. S. 2011, The Astrophysical Journal, 732, 61, doi: [10.1088/0004-637X/732/2/61](https://doi.org/10.1088/0004-637X/732/2/61)
- Zuckerman, B., & Song, I. 2004, ARA&A, 42, 685, doi: [10.1146/annurev.astro.42.053102.134111](https://doi.org/10.1146/annurev.astro.42.053102.134111)
- Zuckerman, B., Song, I., Bessell, M. S., & Webb, R. A. 2001, ApJL, 562, L87, doi: [10.1086/337968](https://doi.org/10.1086/337968)